Journal of Sound and Vibration (2001) **247**(2), 243–260
doi:10.1006/jsvi.2001.3668, available online at http://www.idealibrary.com on IDEAL®

ESTIMATION OF PARTIAL DISCHARGE PARAMETERS IN GIS USING ACOUSTIC EMISSION TECHNIQUES

N. GUPTA† AND T. S. RAMU

Department of High Voltage Engineering, Indian Institute of Science, Bangalore 560012, *India*

(*Received* 25 *February* 2000, *and in final form* 26 *February* 2001)

Conventional electrical techniques for the monitoring of partial discharge (p.d.) activity in enclosed systems like gas insulated substations (GIS) have certain inherent limitations, which has prompted the exploration of non-electrical techniques. Acoustic detection of p.d. in a GIS is based on the retrieval and analysis of mechanical signals produced on the walls of the metallic enclosure due to electrical discharge activity within. A theoretical modelling of the process by which a discharge produced within the GIS sets up detectable signals on the walls of the enclosure seems to be lacking. The present work consists of the development of a model for the propagation of electrically induced acoustic waves through gaseous medium, and their effect on the walls of the GIS, giving adequate representation to fluid–structure coupling. A numerical simulation of the process is shown to yield important information about the proper type of instrumentation required for such non-invasive tests, and aid in designing robust strategies for locating the source of the discharge.

© 2001 Academic Press

1. INTRODUCTION

Gas insulated systems (GIS) are being increasingly preferred over conventional air insulated systems in high-voltage applications. Typically, such systems consist of an enclosed structure filled with a pressurized gas. The possibility of using a gas like SF_6, with insulating properties superior to air, make such systems much more compact, safe and reliable compared to conventional ones. However, as the systems are enclosed, non-invasive maintainence methods of such systems assume importance.

Among the more important tests to establish the integrity or otherwise of a dielectric system such as a gas insulated substation, partial discharge (p.d.) measurements are known to reveal certain gross defects. Partial discharges are nanosecond scale discharge phenomenon which occur typically in regions of high electrical stress concentration. The presence of inherent defects within the components of the GIS, for example, metallic protrusions, free metallic particles, etc., are common causes of partial discharges. Electrical or direct partial discharge measurements have been in use for quite some time now, and their usefulness has sufficiently been emphasized. Detection of partial discharge activity in fully enclosed systems using electrical methods have certain disadvantages: the methods are invasive and the measured data is often suspect due to the fact that p.d. signals are infected by considerable electrical noise which affect both the magnitude and the shape of the discharge signals. They also need auxilliary power sources and measuring equipment

†Current address: Department of Applied Physics, Eindhoven University of Technology, 5600MB Eindhoven, The Netherlands.

0022-460X/01/420243 + 18 $35.00/0 © 2001 Academic Press

besides an electrically sterile environment. In the recent past, non-electrical techniques have come into existence, one of them being the acoustic detection technique. This method of measurement is non-invasive, immune to electro-magnetic interference, and needs only very simple instrumentation like acoustic sensors and pre- and post-amplifiers in the frequency ranges of a few tens of kHz to about 500 kHz.

The acoustic method of p.d. detection is based on the retrieval and analysis of the acoustic signals and establishment of a correlation between them and the partial discharges to which they are due. Electrical discharge activity within a GIS causes pressure waves to be set up in the insulating fluid environment, which propagate to the walls of the GIS chamber to set up small-amplitude vibrations. The signals thus generated can be detected with appropriate acoustic sensors placed on the external surface of the GIS enclosure. The shape and amplitude of the signals arriving at different locations on the walls of the chamber depend on various factors like propagation path and properties of the fluid medium and the material of the enclosure walls. Graybill *et al.* [1] described measurements of audio-signals from p.d. in GIS using a hand-held acoustic probe. Acoustic spectrum signatures of electrical discharges in different power equipments have been reported in some detail by Harrold [2]. Owing to excessive pollution of signals caused by background noise in the audio-frequency range, the emphasis gradually shifted to studies in the ultrasonic band [3]. Lundgaard *et al.* [4] developed the theoretical aspects of acoustic signal propagation in GIS due to p.d., and attempted to correlate the experimental findings with theoretical expectations [5]. Laboratory tests as performed by them are prohibitively expensive in terms of time and money, and difficult to perform on power apparatus in service as the associated parameters are not easy to control.

Certain issues connected with the acoustic method of p.d. detection within a GIS have not been adequately addressed in the existing literature. An understanding of the complicated way in which pressure waves propagate from the discharge source and convert to mechanical waves on reaching the enclosure wall has not been rigorously studied. The types of mechanical waves (flexural, semi-longitudinal, etc.) that are to be expected to dominate the registered signal also depend on the frequency range in which the measurements are made.

In order to be able to design the instrumentation for acoustic emission detection, and for an effective choice of sensors, it would not only be advantageous, but often necessary to model, simulate and estimate by direct computation, the probable acoustic emission signals realizable at the walls of the enclosure. Physically realistic models also serve to identify the source, if any, of spurious signals during experimentation.

An important advantage of the acoustic emission technique is its ability to yield information about the location of the source of discharge within the GIS structure. A thorough knowledge of the frequency ranges and attenuation characteristics of the waves that can be set up in the GIS structure by discharge-induced pressure pulses is necessary in order to design a robust strategy for localizing the source of a discharge. A simulation model of the process could also aid in gaining such insight.

In the first part of this paper, experiments are performed to capture the nature of the pressure waves generated by partial discharges. Using these waveforms as input, the physical process of acoustic wave propagation through the gaseous medium and the metallic wall is modelled in the second part of the paper. This leads to a coupled set of equations governing the fluid–structure interaction problem, which is solved by the finite element technique. Experiments are then performed on a model GIS structure, to study the validity of the numerical model. The results and insights gained from this attempt are outlined in section 4 of the paper.

2. PRESSURE PULSE MEASUREMENTS

The numerical model requires the pressure–time variation due to the p.d. pulse as an input. The nature of the pressure pulse generated due to a corona discharge is difficult to predict theoretically. Sound pressure pulses set up in the immediate vicinity of p.d. are similar in form to the shock wave generated by the point explosion following a fast concentrated energy release [6] and any accurate prediction would involve the solution of coupled partial differential equations of gas dynamics which are often non-linear, along with appropriate equations governing the production of charged particles due to the discharge activity. In this work, a simpler alternate method is adopted. An experimentally obtained pressure–time record has been used as an input to the numerical simulation. However, since the aim of this paper is the study of discharges based on signals obtained in the 20–250 kHz range, the experimental time-signal was filtered to remove the higher-frequency components. This pressure pulse, obtained from the experimentally obtained pulse by appropriate filtering, is imposed at the point of the corona discharge and it is assumed to behave as a spherically symmetric source of acoustic disturbance.

A standard hydrophone also suitable for measurements in air, of Type 8101 of Brüel & Kjær (1 Hz–125 kHz range) was used. Although this sensor has a flat response curve up to 125 kHz, it possesses considerable response well into the megahertz range. The acoustic measuring circuit and data acquisition circuit were both electrically isolated from the remaining part of the circuitry. The partial discharge detector, of the ERA (Model-5) make, with an elliptic display was used in conjunction with a tuned impedance with a tuning range of 2–50 pF (also of the ERA make) for the partial discharge measurements. The measurements were performed in a shielded room to eliminate external electro-magnetic interference. The detector and test-circuit were calibrated using a Bonar Instruments two-pulse calibrator Type 756 with a selectable pulse output range of 5–500 pC. All measurements have been performed several times in order to check the repeatability and reproducibility of the data.

Figure 1(a) shows a typical pressure pulse measured by a pressure transducer due to a corona pulse of magnitude 184 pC.

The hydrophone was placed at a distance of 20 mm from the source of discharge. The ordinate in the figure represents 'normalized pressure', i.e. $p(t)/p_{max}$, where $p_{max} = \max(p(t))$. Figure 1(b) shows the corresponding frequency spectrum. It should be noted that though the pressure sensor has considerable response in the megahertz range, it is the response in its

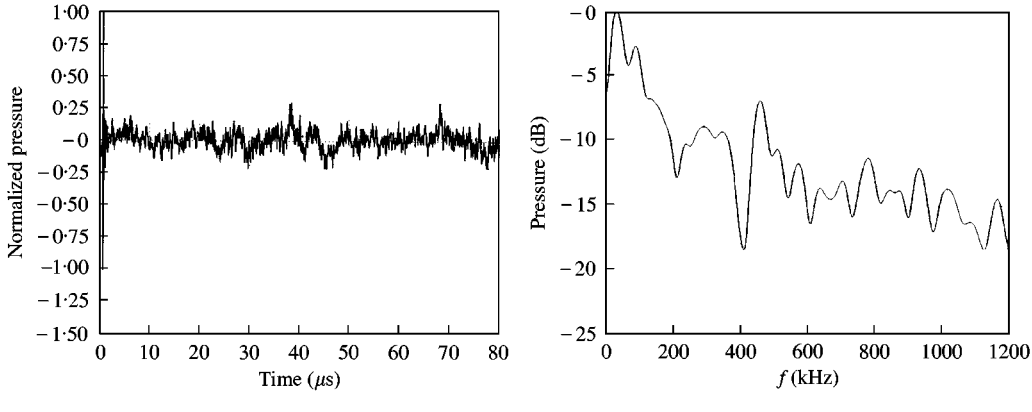

Figure 1. (a) Typical pressure pulse (obtained experimentally) for a discharge magnitude of 174 pC, and (b) frequency spectrum of pressure pulse.

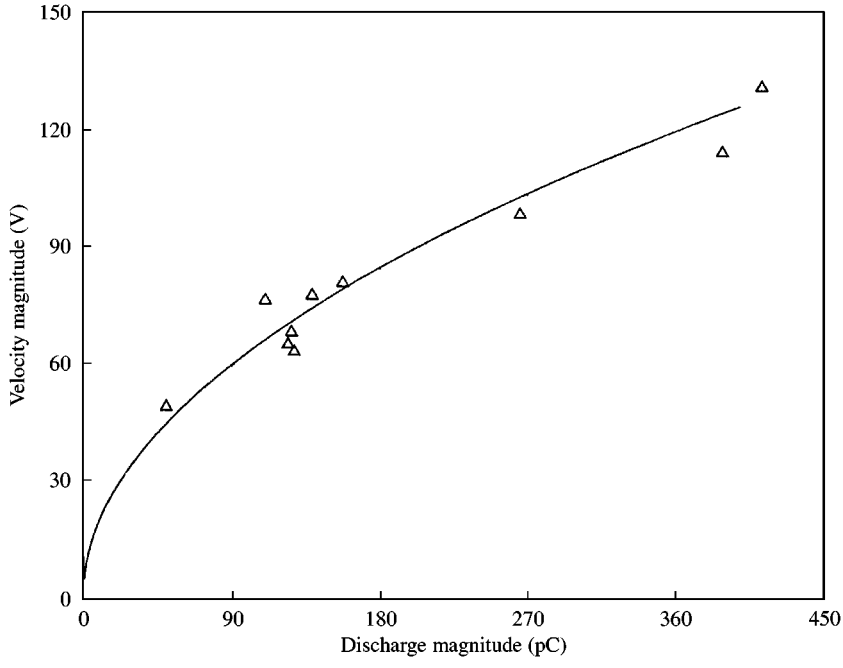

Figure 2. Velocity as function of discharge magnitude: △; experimental data in air. The solid line represents the best fit in the form $Y = AX^{0\cdot6}$ to the data.

rated frequency range which is most accurately captured by the sensor. It may be seen from Figure 1(b) that the signal exhibits a broadband spectrum with the maximum response appearing within 20–250 kHz. Some higher-frequency components are seen to exist, some of which may be due to amplifier noise. However, in the present case, studies have been concentrated in the frequency range of 20–250 kHz with an aim to use signal response in this range for partial discharge detection.

As mentioned earlier, the pressure pulse shown in Figure 1(a) is obtained for a discharge magnitude of 184 pC. It was assumed that with an increase in the magnitude of the discharge, the frequency content of the pressure pulse remains unaffected while the amplitude increases. To understand the manner in which the peak pressure scales with the magnitude of the discharge, simultaneous acoustic and electrical measurements were made to correlate the maximum amplitude of the pressure pulse and the magnitude in pC of the discharge causing it. Figure 2 shows the corresponding results for air at atmospheric pressure. A fit of the form $y = ax^b$ was made to the experimental data. A non-linear least-squares technique with this scaling relation yields a value of $b = 0\cdot6$ for air. Similar experiments performed in Nitrogen and SF_6 yield values of $b = 0\cdot8$ and $1\cdot1$ respectively. These scaling relationships provide means of obtaining, for input to the numerical model, pressure pulses at varying magnitudes of the discharge in different insulating gases.

Moreover, a justification for the assumption of a spherically symmetric source of disturbance is provided by Figure 3. Hydrophones placed radially around the source have been used to simultaneously capture the signals emitted in different directions. The nearly invariant nature of the pressure signal with respect to the angular position of the sensor as shown in Figure 3 indicates that the assumption of a radially symmetrical spherical wave propagation from the source point is generally valid, in any case, up to about 75 kHz. Lim [7] has suggested that above 30 kHz, the omni-directional quality of the pressure wave is

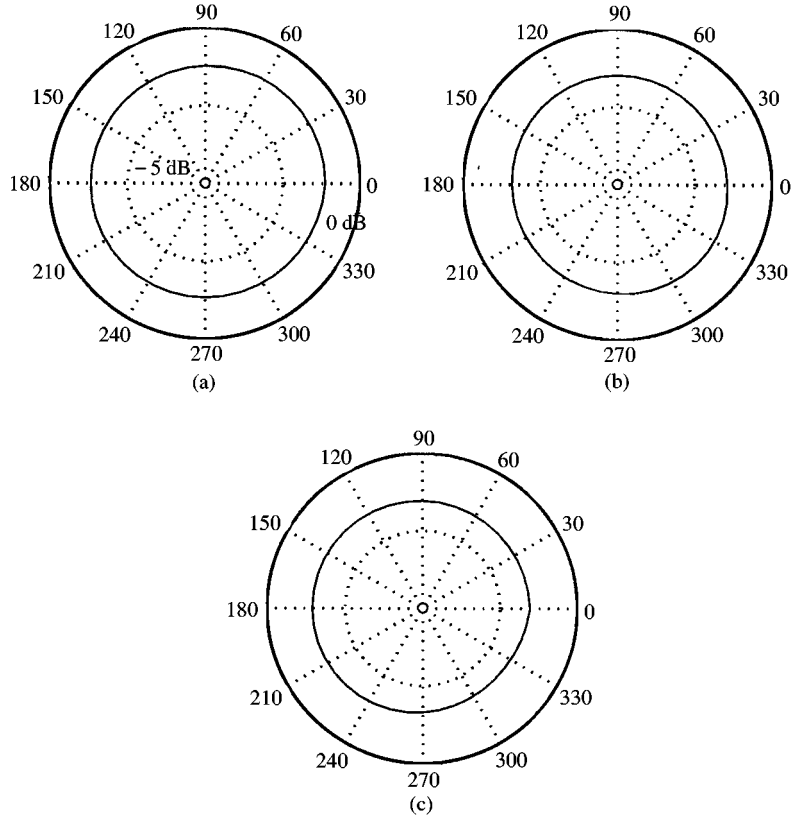

Figure 3. Polar plot (at same scale) showing directivity of the pressure signal at (a) 30 kHz, (b) 50 kHz and (c) 75 kHz.

lost, mainly due to diffraction at the electrodes. Bengtsson *et al.* [8] have recently used multiple acoustic sensors to investigate the possible causes for the statistical deviations from a simple proportionality between acoustic and electric p.d. signal levels in power transformers, and have attributed it to statistical variations in the angular distribution of the acoustic energy emitted from the discharge site. Figure 3 indicates that the loss of directionality as measured in the present work is not very pronounced; it is however possible that a more pronounced effect would have been noted if a larger number of hydrophones had been used.

The above measurements were made in air in order to get an idea about the frequency content of the acoustic waves generated by the partial discharge event. The acoustic waves generated in other gases like SF_6 ro N_2 would be qualitatively similar, though these gases could absorb some higher frequencies. The damping effect of the insulating medium on the acoustic wave is not taken into consideration in this work.

3. THE THEORETICAL MODEL

The pressure wave is assumed to be radially symmetric in nature. The spherical wave radiates out towards the surface of the GIS enclosure and on striking it, acoustically couples with it and sets up small-amplitude vibrations. These small-amplitude vibrations are

recorded by acoustic sensors placed at various locations on the external surface of the enclosure. Typically, a spherical longitudinal wave (also called compressional wave) travels through the gaseous insulating medium at a constant wave velocity characteristic of the gas in question. The waves that are set up in the enclosure walls can be thought of as being composed of both longitudinal and shear waves (also called flexural waves). The longitudinal waves travel faster than the shear waves. An additional complication arises when the wavelength of the travelling waves are comparable to the enclosure wall thickness. Due to repeated reflection at the free surfaces, standing wave patterns develop along the thickness direction and the speed of propagation becomes dependent on the frequency. In other words, for low enough frequencies and thick enough enclosure walls, dispersive wave propagation takes place along the enclosure.

The assumption of a point source for the numerical simulation model effectively precludes any directionality. However, though not considered in this work, directionality of the source pressure disturbance can be represented by adopting a spherical void within the finite element mesh, and ascribing statistically varying pressure magnitudes at various nodes on the surface of the void.

The propagation of the acoustic wave outwards from the spherically symmetric partial discharge source is described by

$$\nabla^2 p - \frac{1}{c^2}\frac{\partial^2 p}{\partial t^2} = -\rho f(t)\delta(x - x_0)\delta(y - y_0)\delta(z - z_0), \tag{1}$$

where c is the velocity of sound in the fluid and ρ is its density. The function $f(t)$ represents the volume acceleration due to a point source located at (x_0, y_0, z_0), and δ denotes the delta function. The nature of the gas affects the above equation through the density ρ, or the characteristic wave velocity in the gas. The density of the gas is a function of the pressure inside the GIS chamber and should be appropriately derived from the equation of state for the gas used.

The motion of the structure obeys the equation of equilibrium,

$$\sigma_{ij,j} = \rho_s \ddot{u}_i, \tag{2}$$

where σ_{ij} denotes the stress tensor, ρ_s the density of the solid and $\ddot{u}$ the acceleration. In addition, the wave propagation in the structures is elastic in nature, and as a result a linear relation,

$$\sigma_{ij} = \mathscr{L}^e_{ijkl}\varepsilon_{kl}, \tag{3}$$

describes the relation between the stress σ_{ij} and the strain ε_{ij}. The constitutive tensor $\mathscr{L}^e_{ijkl}$ can be written as

$$\mathscr{L}^e_{ijkl} = \frac{E}{2(1+\nu)}\left[(\delta_{ik}\delta_{jl} + \delta_{il}\delta_{jk}) + \frac{2\nu}{1-2\nu}\delta_{ij}\delta_{kl}\right], \tag{4}$$

where E is the Young's modulus and ν the Poisson ratio of the material of the enclosure and δ_{ij} represents the Kronecker delta.

The coupling between equations (1) and (2) are caused by the equation describing the interface, which is given by

$$n_i \ddot{u}_i = -\frac{1}{\rho} n_i \frac{\partial p}{\partial x_i} \tag{5}$$

and relates the acceleration normal to the surface to the variation of the pressure in the same direction.

The fluid structure interaction model proposed here solves the equation for acoustic wave propagation (equation (1)) along with the equation for elastic wave propagation in structure (3). This is a more general approach as opposed to treating the enclosure as a thin shell, which would mean that only flexural waves might be supported. It is not appropriate to make such an assumption in the present case because the information about the discharge magnitude and location is carried by the transient part of the signal, which necessarily contains the high-frequency components. This will be further discussed in section 6.

It is evident that this theoretical model ultimately translates into a fluid–structure interaction problem involving solution of the coupled partial differential equations (1) and (2) subject to the boundary condition given by equation (5). The 3-D domain is discretized into elements with the following equations being valid over each element:

$$\mathbf{M}_f\ddot{\mathbf{P}} + \mathbf{K}_f\mathbf{P} = \mathbf{R}_{sf} + \mathbf{F}_f, \qquad \mathbf{M}_s\ddot{\mathbf{U}} + \mathbf{K}_s\mathbf{U} = \mathbf{R}_{fs}. \tag{6}$$

In the above equations, $\mathbf{M}_f$ and $\mathbf{M}_s$ are the usual finite element mass matrices and $\mathbf{K}_f$ and $\mathbf{K}_s$ are the stiffness matrices for the acoustic and the solid domains respectively. If the shape functions for the acoustic elements and the solid elements are $\mathbf{N}_f$ and $\mathbf{N}_s$, respectively, then the corresponding matrices, defined over the volumes of the elements V_f^e and V_s^e, are given by

$$\mathbf{M}_f = \frac{1}{c^2}\int_{V_f^e} \mathbf{N}_f^{\mathrm{T}}\mathbf{N}_f\,\mathrm{d}V, \qquad \mathbf{K}_f = \int_{V_f^e} \nabla\mathbf{N}_f^{\mathrm{T}}\nabla\mathbf{N}_f\,\mathrm{d}V,$$

$$\mathbf{M}_s = \rho_s\int_{V_s^e} \mathbf{N}_s^{\mathrm{T}}\mathbf{N}_s\,\mathrm{d}V, \qquad \mathbf{K}_s = \int_{V_f^e} \nabla\mathbf{N}_s^{\mathrm{T}}\nabla\mathbf{N}_s\,\mathrm{d}V. \tag{7}$$

The vectors $\mathbf{P}$ and $\mathbf{U}$ contain the nodal pressures and nodal displacements for the acoustic and the solid elements. The force vector $\mathbf{F}_f$ arises from the volume velocity of the discharge, while the interface force vectors $\mathbf{R}_{sf}$ (due to the structure on the acoustic element) and $\mathbf{R}_{fs}$ (due to the fluid on the structure) are only applicable to the elements at the fluid structure interface. Following Zienkiewicz and Bettess [9], for an acoustic element sharing an interface S^e (having an outward normal $\mathbf{n}$) (see Figure 4) with a solid element, $\mathbf{R}_{sf}$ is defined as

$$\mathbf{R}_{sf} = -\int_{S^e} \mathbf{N}_f^{\mathrm{T}}\rho\mathbf{n}\cdot\mathbf{N}_s\ddot{\mathbf{U}}_s\,\mathrm{d}S, \tag{8}$$

and, for the corresponding adjacent solid element, $\mathbf{R}_{fs}$ is defined as

$$\mathbf{R}_{fs} = \int_{S^e} \mathbf{N}_s^{\mathrm{T}}\mathbf{n}\cdot\mathbf{N}_f\mathbf{P}\,\mathrm{d}V. \tag{9}$$

In the above equations $\cdot$ denotes the usual vector dot product.

The computational procedure followed is a semi-discretization method in that it employs both the finite element and finite difference (FD) approximations. The governing p.d.e.s are discretized in space by the finite element method (FEM) to obtain a set of ordinary differential equations as given below, which are then integrated in time by an FD scheme [9, 10]. Eight noded brick elements are used to discretize the fluid and 20 noded bricks are

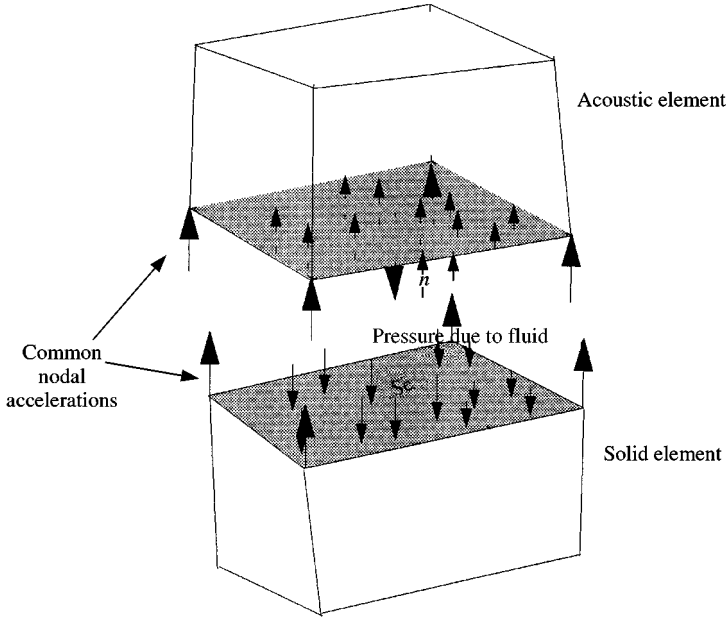

Figure 4. Schematic showing a typical acoustic and solid element and the interaction between them. The shaded faces lie on the shared interface.

used to discretize the solid enclosure. The 20 noded elements with quadratic shape functions are known to be better suited to modelling the flexural response. The central difference method is used to integrate the discretized equations of motion in time. A time step size smaller than that dictated by the Courant stability limit is used in the computations.

As attention is focussed on the early part of the signal, i.e. the transient period before reflections from the flanges corrupt the original response of the structural enclosure, the length of the time signal which is useful is then determined by the time required for reflection from the flanges, and therefore by the dimensions of the enclosure. Finally, it must be mentioned that the present paper concentrates on the response due to a single p.d. event. Response to a p.d. pulse train may be obtained by convolution of the pressure signals due to single events as outlined in reference [10].

4. EXPERIMENTAL SET-UP

The objective of the experimental measurements were to check the validity of the theoretical model proposed and to assess its applicability in understanding acoustic wave propagation in a GIS.

The dimensional diagram of a model GIS with sensors mounted on the walls is given in Figure 5(a). The stainless-steel, leak-proof chamber is of a rectangular cross-section with dimensions 600 mm × 300 mm × 300 mm. On the central h.v. conductor there are finely drilled re-entrant holes to accomodate needles with different tip-radii (100–500 μm). This is to simulate protrusions on the high-voltage conductor, and hence p.d. (corona) sources. The needles are connected to a high-voltage (h.v.) source (60 kV, 150 kV A, single-phase transformer). A circular glass window on one side of the chamber provides a view of the interior. The model is fully equipped with both vacuum and pressure gauges to monitor the

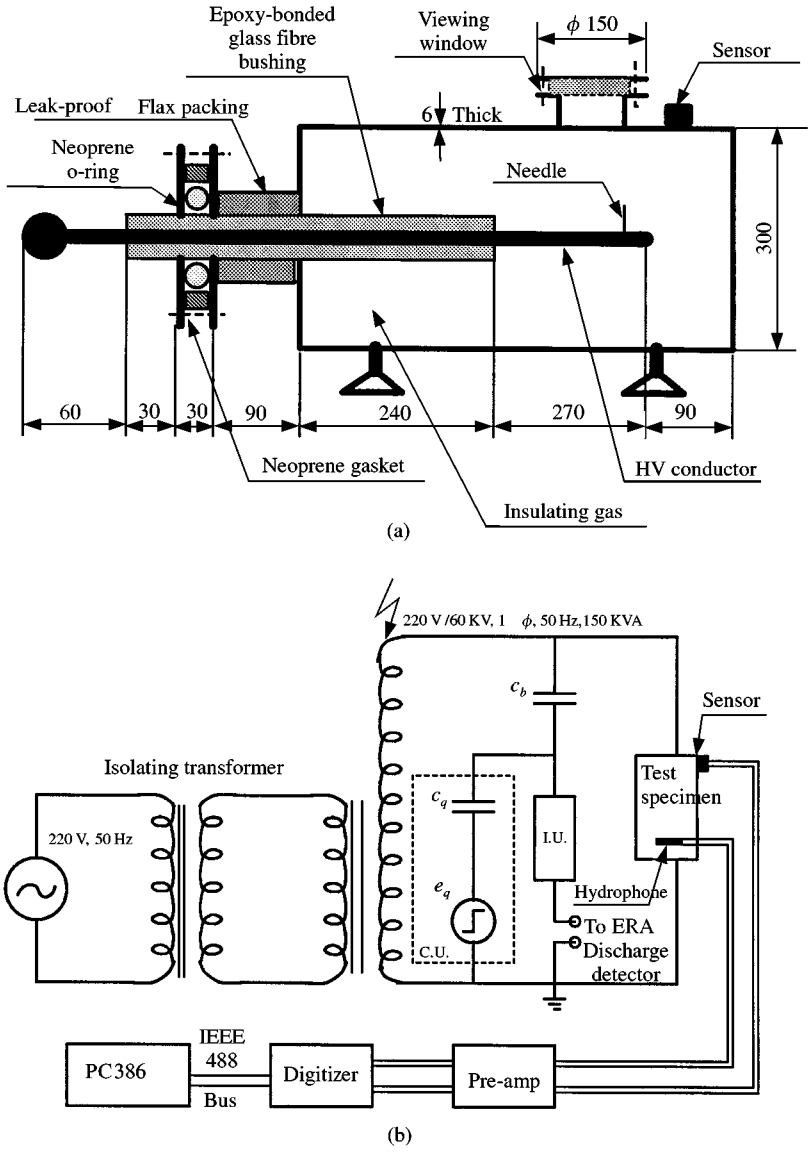

Figure 5. (a) Model GIS and (b) schematic circuit diagram for the experimental set-up. $C_q = 2$ pF, $C_b = 4400$ pF, I.U. = Input Unit 2 (matching impedance) and C.U. = calibrating unit.

pressure. A high capacity vacuum pump was used to evacuate the GIS chamber to a pressure of about 10^{-3} Torr before filling it with (1) nitrogen gas and (2) SF_6 gas to pressures between 1·0 and 3·0 atm.

The acoustic measurements were made using velocity sensors fixed to the wall of the model GIS chamber. These are piezoelectric sensors of PAC WD make (wide-band with range 10–1000 kHz), R6D (peak sensitivity at 60 kHz) and R15D (peak sensitivity at 150 kHz).

The signals measured by the acoustic sensors were fed into a dual-channel digitizer of Sony Tektronix, RTD 710A make, with a maximum sampling rate of 10 ns. The digitizer was in turn connected to a PC via the IEEE-488 bus; waveforms recorded by the digitizer

were stored in the PC for analysis. Simultaneous electrical partial discharge measurements made using the ERA discharge detector were also digitized and stored in the PC similarly. The schematic circuit diagram is shown in Figure 5(b).

The detector and the test circuits were calibrated using a Bonar Instrument's two-phase calibrator type 756 with a selectable pulse (magnitude) output range of 5–500 pC.

A few words about the measurement procedure would be in place here. The sensors can only detect velocities perpendicular to the surface to which they are attached. Hence, longitudinal waves are detected and not the shear waves. The coupling of ultrasound between two media depends on their respective acoustic impedances and the resulting reflection of ultrasound at the media interface. It should be ensured that the sensor's surface is smooth and clean, allowing for maximum couplant adhesion. The application of a couplant layer should be thin, so it can fill the gaps caused by surface roughness and eliminate air gaps to ensure good acoustic transmission. The sensor should be held firmly to the testing surface at all times. Commonly used couplants are vaccum greases, water-soluble glycols, solvent-soluble resins and other proprietary ultrasonic couplants. In this case, silicon grease was used.

5. VALIDATION OF THE NUMERICAL MODEL

The pressure wave generated by the discharge at a point in the insulating fluid travels to the enclosure wall and sets up small amplitude vibration of the surface of the enclosure. The velocity of the vibrating enclosure registered by a piezoelectric surface sensor is stored in a computer via a digitizer. These experimentally obtained results are compared to those of numerical runs under similar simulated conditions, with a view of validating the simulation model.

Attention is focussed on the initial transient signal as opposed to the stationary waves set up after many reflections from the flanges. Figures 6(a) and (b) show a typical velocity pulse and its associated frequency spectrum in the GIS chamber with air at atmospheric temperature and pressure as the insulating medium. As in the case of the pressure signal measured by a hydrophone (see Figure 1(b)), the velocity signal also exhibits a broadband frequency spectrum with frequencies ranging from 20 to 250 kHz. This indicates that most of the frequencies present in the pressure wave striking the walls of the structural enclosure are retained in the waves propagating through them.

The velocity signal that would be realizable at a point on the external surface of the enclosure wall as calculated through a computer simulation using the theoretical model described in section 3 is superposed on the experimentally obtained signal in Figure 6. It can be seen from the above figures that the experimentally and numerically obtained results match reasonably well. For the experimentally obtained curve, the ordinate in Figure 6(a) is normalized as $\hat{\dot{u}}_{exp} = \dot{u}(t)/\dot{u}_{max}$, where $\dot{u}(t)$ is the velocity in V measured by the data acquisition system, and $\dot{u}_{max} = \text{maximum}(u(t))$. In the numerical computations, $\dot{u}(t)$ is obtained in units of m/s, but when similarly normalized as $\hat{\dot{u}}_{num} = \dot{u}(t)/\dot{u}_{max}$, it is possible to plot both the numerically and experimentally obtained results on a common scale of $[-1, 1]$. The frequency spectrum shown in Figure 6(b) uses the values of $\hat{\dot{u}}_{exp}$ and $\hat{\dot{u}}_{num}$ for the computations. The presence of some high frequencies may be detected in the experimental data which are not present in the numerically obtained signals; this could be because of numerical dispersion due to the use of the central difference method, since this method is unable to negotiate sharp variations. Also, the dimensions of the finite element mesh decide the maximum characteristic eigenfrequencies it can support, and higher-frequency resolution can be obtained by employing a smaller mesh size; this would

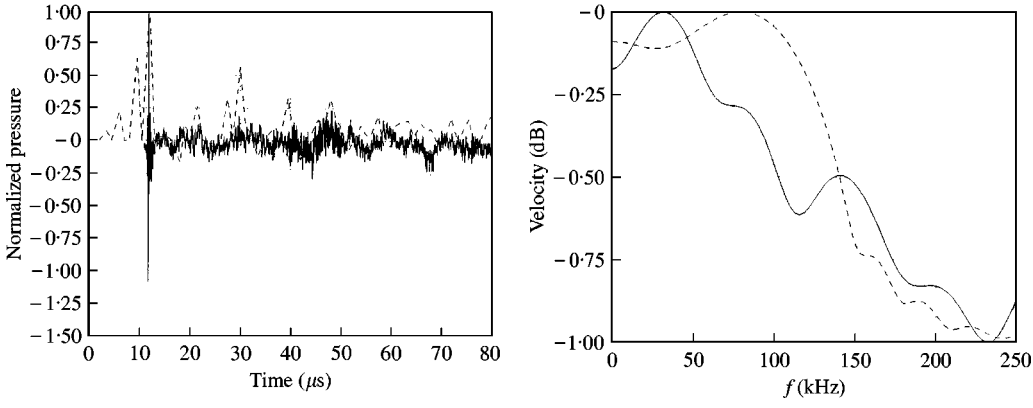

Figure 6. (a) Typical experimental velocity signal (——) in model GIS. The source height is 135 mm and the sensor is directly under the source; numerically obtained velocity signal (- - -). (b) Typical frequency spectrum (——) of experimentally obtained velocity signal in model GIS; numerically predicted frequency spectrum (- - -).

considerably increase the computational time and cost. This does not seem necessary in view of the fact that in the frequency range of interest, the match between the experimental and numerical spectra seems reasonably good. Moreover, the experimental data may also contain some spurious noise.

Any acoustic wave would undergo attenuation, mainly due to geometrical spreading of the wave, as well as absorption, as it progresses through the gaseous medium away from the point of inception; a further reduction occurs as the wave progresses along the surface of the enclosure. The effect of the variation of the following parameters on the ultimate velocity signal amplitude detectable on the enclosure surface is studied here: (1) height of the source of corona discharge H above the surface of measurement and (2) the distance of the point of measurement (i.e., sensor location) d from the point at which the pressure wave first strikes the surface. Again, experimentally and numerically observed attenuation patterns are compared for similar positions of the source and the sensor. This exercise provides a further check on the validity of the numerical model.

Figure 7 shows the attenuation of the velocity signal in dB at a given sensor location with increase in the height of the corona source above the plate on which the sensors are mounted. It may be noted that for calculating the attenuation with height of source, the peak velocity v_{ref} obtained at a point on the plate, due to a source placed at a height 10 mm directly above it, is used as a reference value. Figure 7 pertains to the results for the case where the sensor position remains fixed at a point directly beneath the corona source. Thus, the attenuation observed could be attributed solely to the variation in H. It can be seen from the numerical data, that with an increase in height H of the source of corona discharge above the surface on which the sensor is attached for detection, the signal amplitude diminishes at an approximately constant rate per unit of normalized height ($\hat{H} = H/L$, where L is a characteristic length of the GIS chamber). The experimental data plotted against normalized height matches reasonably well with numerical data except at larger values of $\hat{H}$ ($> 0{\cdot}15$). This could be due to the fact that when the source is too high above the enclosure, the amplitudes of the signals detectable at the sensor location is very small due to scattering and wave spreading.

Figure 8 depicts the attenuation of the velocity signals in dB obtained experimentally and numerically, with varying sensor distance from the source. The attenuations in both the cases were measured with respect to v'_{ref}, the velocity at a point on the enclosure directly

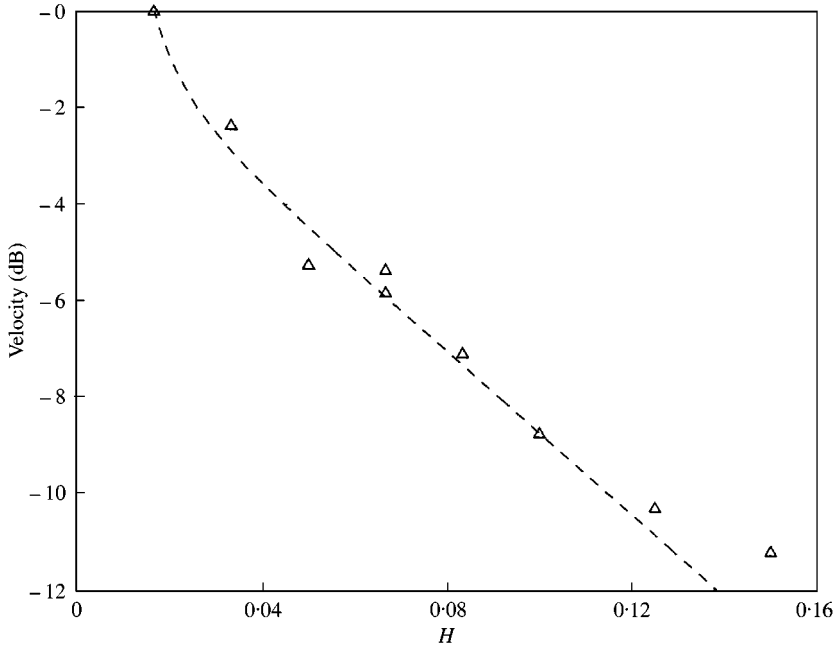

Figure 7. Attenuation of velocity signal with increasing height of corona source obtained numerically (- - -); △; experimental data.

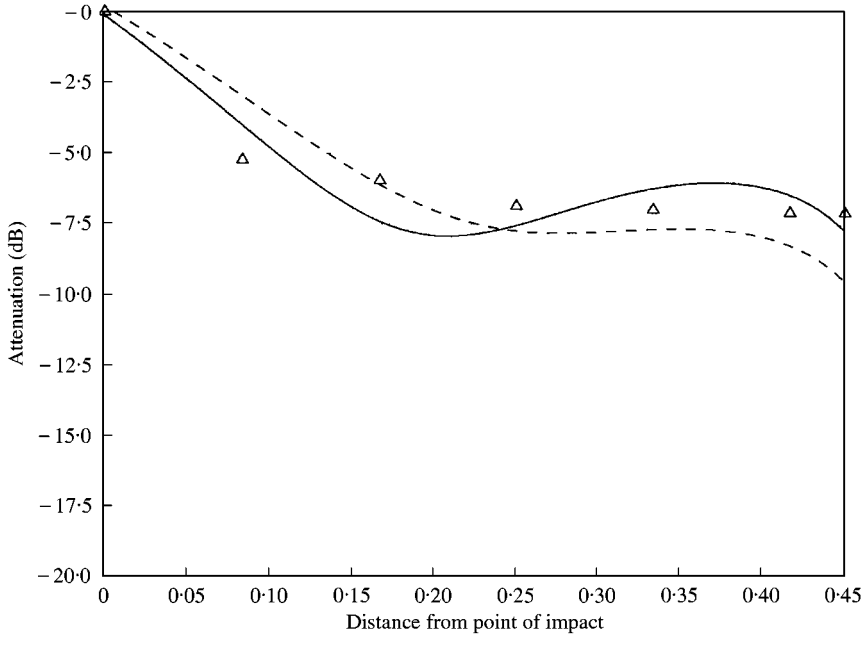

Figure 8. Attenuation with sensor distance from the corona source: △; experimental data; ——; numerical prediction. The solid line represents a model fit to the data.

beneath the point of discharge inception. The amplitude of the signal is seen to fall off with an increase in distance from the source. A third order polynomial of the form $Y = A_1 + A_2X + A_3X^3$ fitted to the experimental data by least-squares regression is seen to closely approximate the numerical data in Figure 8. (It should be noted that the nature of the fit is arbitrary and not based on any physical reasoning.) Thus, the amplitude of the signal falls off with distance both in the fluid medium, as well as in the structural medium of the enclosure wall, and this aspect is seen to have been captured reasonably well by the numerical model.

It should be noted that the propagation of the pressure wave through the gaseous insulating medium is non-dispersive in nature. However, the propagation of the mechanical waves through the enclosure structure is dispersive in nature and different frequency components travel with different velocities. The close match between experimentally and numerically obtained attenuation characteristics imply that the numerical model is able to model both the non-dispersive propagation in the gas as well as the more involved dispersive propagation in the solid enclosure.

6. DISCUSSION

In this section, the nature of the signals captured by the piezoelectric surface sensors are analyzed. As will be seen later, such insight might be useful in choosing appropriate sensors and deciding on proper localization techniques under field conditions.

Wavelet transform techniques have been used for this purpose. Since the wavefront carries the most important information about the discharge causing it, the velocity signals of interest are non-stationary in nature. Hence, wavelet techniques are deemed as suitable for their analysis.

The continuous wavelet transform is defined as

$$\Psi(\tau, s) = \frac{1}{\sqrt{|s|}} \int x(t)\psi^*\left(\frac{t-\tau}{s}\right) \mathrm{d}t. \tag{10}$$

As seen from the above equation, the transformed signal is a function of two variables, τ and s, the translation and scale parameters respectively. $\psi(t)$ is the transforming function and is called the mother wavelet, and the functions with different regions of support that are used in the transformation process (basis functions) are derived from this main function i.e. it serves as a prototype for generating other window functions. The term "wavelet" means a small wave: the "wave" refers to the condition that this function is oscillatory, and the smallness refers to the condition that the function is of finite length (compactly supported). The translation τ is related to the location of the window, as the window is shifted through the signal, and obviously corresponds to time information in the transform domain. The parameter scale s corresponds to the degree of detail in the signal i.e. high scales (low frequencies) correspond to a non-detailed view or global information of a signal, and low scale (high frequencies) corresponds to a detailed information of a hidden pattern in the signal (that usually lasts for a relatively short time).

It has been shown [11] that the local maxima of the wavelet transform modulus detect the locations of transients or singularities in a signal. In Figure 9, the analyzed signal is a normalized velocity signal as detected by an acoustic emission sensor placed on the surface of the enclosure of a GIS, similar to that shown in Figure 6(a). The abscissa denotes the sample number, the sampling rate being 100 ns. A continuous wavelet transform of the entire signal consisting of 8192 samples was taken. The mother wavelet used is of the type

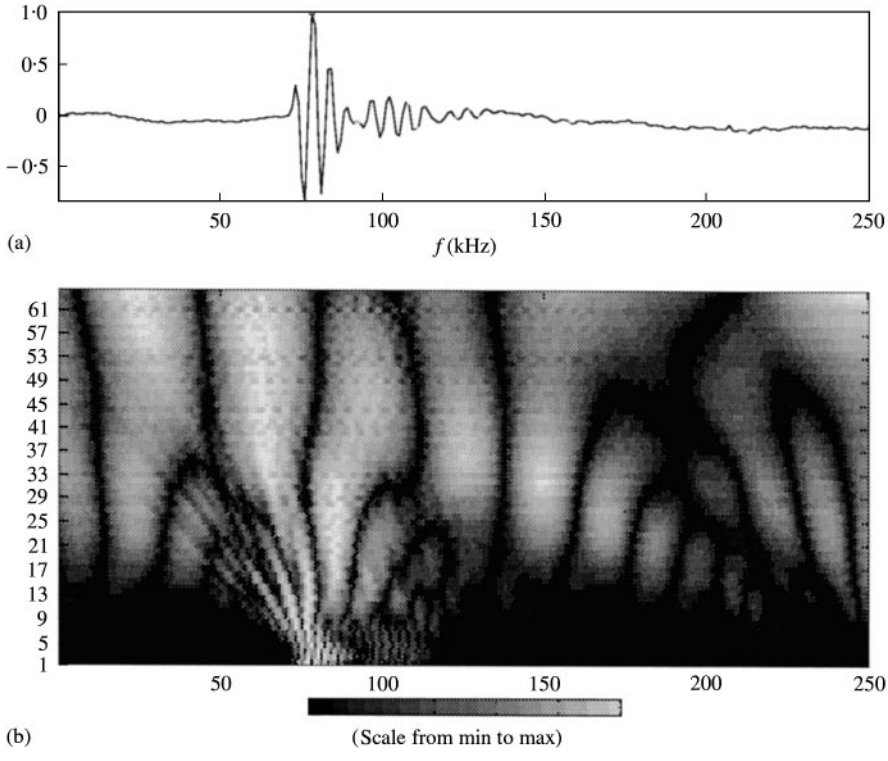

Figure 9. Continuous wavelet transform coefficients for a typical velocity signal: (a) velocity signal, (b) continuous wavelet transform.

"db5" belonging to the Daubechies wavelet family. The scale is allowed to vary from 1 to 64 in steps of 1. In Figure 9, the wavelet transform coefficients have been plotted on the translation-scale plane in the form of a contour plot. It is seen that the maximum values of the coefficients (indicated by the lightest patches) occur predominantly at the time of appearance of the signal due to the partial discharge. They occur at low values of the scale, and hence correspond to higher frequencies. These high frequencies are concentrated within a small time interval indicating that certain frequencies which are present only during the duration of the acoustic "event" may be isolated. These frequencies die out rapidly, as indicated by the dark patches along the rest of the abscissa at small scales. The presence of lighter patches over the translational axis at higher scales indicate the presence of lower frequency components along the entire duration of the record. This kind of time–frequency information obtained using the wavelet transform allows the localization of an 'event' in time, more effectively than a simple time–velocity plot. It is not possible to obtain any such information from Fourier transforms of the signal data.

Hence, the discharge event gives rise to a short lived burst of high-frequency waves and an underlying low-frequency activity which continues for a longer span of time. This underlying low-frequency activity can in fact, be captured by considering only the flexural response of the enclosure structure as has been done in reference [10]. In reference [10], the enclosure has been modelled as a thin shell which can support only flexural waves. Figure 10 shows the frequency spectrum of the velocity response obtained for such an enclosure due to an excitation similar to that shown in Figure 1(a). This frequency spectrum should be compared with Figure 6(b), which shows the response for a more complete

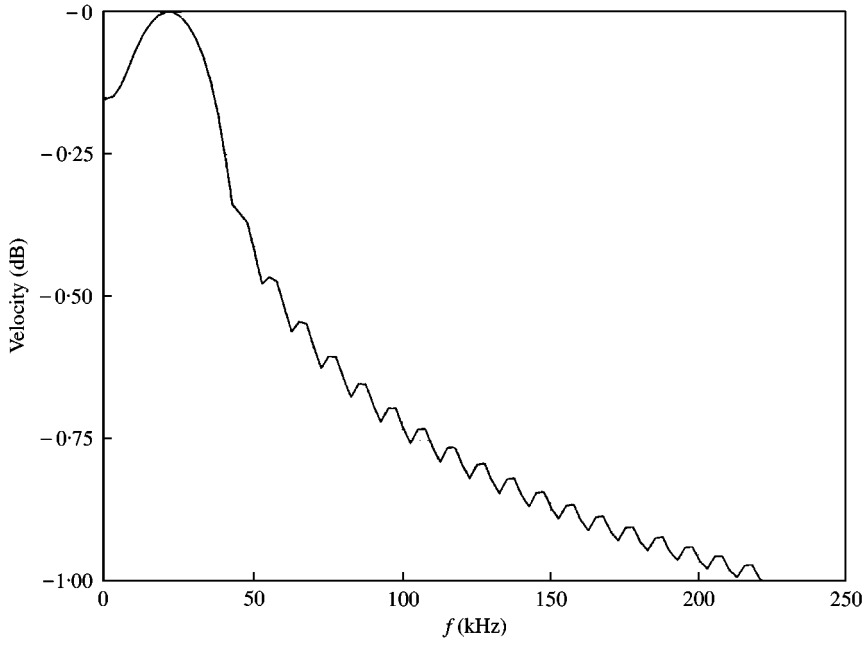

Figure 10. Frequency spectrum of a typical velocity signal obtained numerically using a thin plate (low-frequency) model.

modelling of the frequency response. The thin-shell model shows a peak response at a low frequency of around 20 kHz, while a broadband frequency response is exhibited by Figure 6(b).

To summarize, it may be said that the response of the enclosure structure to excitation due to a partial discharge activity within is of a "dual" nature. The structure responds to the high-frequency components of the pressure pulse like a bulk solid. This implies that the waves, whose wavelengths are small compared to the wall thickness, travel back and forth through the thickness, suffering reflections and mode conversions at the free surfaces. This activity is short lived and can be detected with surface piezoelectric sensors having a flat response in the range of roughly 30–200 kHz. In addition, the low-frequency components of the pressure signal excite flexural waves along the wall. These waves persist for a longer time and can be detected using sensors in the range of < 20 kHz. The signal detected by a broadband sensor, as used in this work, would be the superposition of these two different responses. Resonant sensors in the appropriate range may be used to detect either of the two responses. It should, however, be noted that the frequency ranges over which flexural waves dominate is dependent on the thickness of the wall as well as the material.

A short discussion of how the above observations aid in designing a strategy for determining the location of a discharge would be in order.

The inherent difficulty in formulating a location algorithm that uses only the velocity signals obtained from multiple sensors is the fact that wave propagation through the enclosure wall can be dispersive in nature, i.e., different frequency components may travel at different velocities. Then, the available method of estimating the time delay between signals obtained at different sensor locations due to a single source of discharge is used. The method uses the part of the signal which is not corrupted by the reflections from the flanges or elsewhere. The method of calculation of delay between two recorded signals is detailed

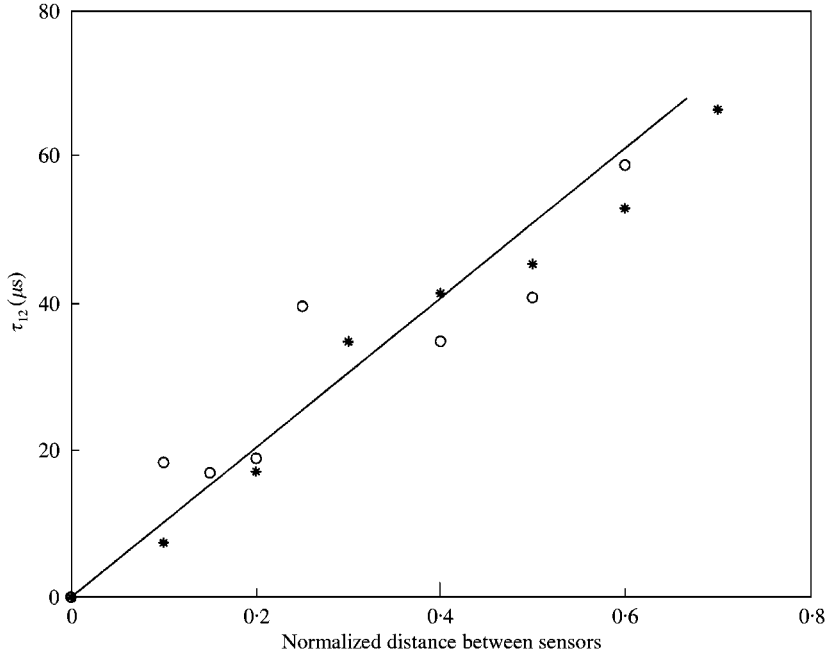

Figure 11. Theoretical prediction of variation of delay with distance between the measuring sensors: **, experimental data; ○, numerical data.

below. S_1 and S_2 are the signals at two sensor positions a distance d apart, such that

$$S_1 = s(t) + n_1(t),\ S_2 = as(t - \tau_{12}) + n_2(t), \tag{11}$$

where n_1 and n_2 are the uncorrelated noise components and τ_{12} the delay between the signals. The maximum value of the cross-correlation function of S_1 and S_2 occurs at $\tau = \tau_{12}$, τ_{12}, being the time delay between the signals. However, this formulation is applicable only in the case of non-dispersive wave propagation. Since, in the present case, the signals are inherently dispersive in nature in the sense that a number of wave components with varying velocities are present, a different approach is necessitated. The time delay also appears in the phase $\Phi(f)$ of the cross-spectral density function of S_1 and S_2 as [12]

$$\Phi(f) = 2\pi f \tau_{12}. \tag{12}$$

For dispersive propagation, if the path difference between S_1 and S_2 is d, τ_{12} may be expressed as

$$\tau_{12} = d/c(f), \tag{13}$$

where $c(f)$ is the frequency-dependent velocity in the material, i.e., in this case, the material of the structural enclosure.

If the function $c(f)$ is known, delays can be obtained at a desired frequency. Low-frequency sensors, therefore, will capture the flexural waves, the wave velocity of which are proportional to the square root of the frequency. The Rayleigh–Lamb equations to determine the function $c(f)$ can also be used as done in reference [13]. On the other hand, if high-frequency sensors are used, the signal will be dominated by the wave components that

travel at almost the dilational wave speed C_L of the material, where C_L is given by

$$C_L = \frac{E(1-\nu)}{\rho_s(1-2\nu)(1+\nu)}. \tag{14}$$

This means that at low frequencies, the detection has to take the dispersive nature of the propagation into account, while at high frequencies, a frequency-independent wave velocity can be used. This has been demonstrated in Figure 11, where sensors with response in the range 100–150 kHz have been used to capture signals at different locations on a face of the GIS enclosure. If interest is confined to the early part of the recorded signal, a first approximation would be to use C_L as the frequency-independent wave velocity. This assumption then justifies the use of a linear fit to the $\Phi(f)$ versus f data in equation (12), for delay calculation from experimental and numerical records. The delays obtained from the slopes of the linear fits were plotted against sensor distance d in Figure 11. The slope of the solid line in Figure 11 represents the delays calculated considering frequency-independent velocity C_L. It can be seen that C_L matches reasonably well with the numerical and experimental data, and may be used as an estimate of the velocity of wave propagation without much loss in accuracy.

7. CONCLUSIONS

The following conclusions can be drawn from the work reported in this paper.

- Acoustic waves emitted from partial discharges can be modelled as radially symmetric, broadband (20–250 kHz) waves.
- The mechanism by which the GIS enclosure is excited by these acoustic waves can be modelled as a fluid–structure interaction problem. A complete modelling of the structure involves treating it as a bulk solid rather than a thin-shell structure. The model has been validated against experimental data and has been found to be adequate.
- Low-frequency sensors will capture only the flexural waves; when sensors with high enough frequency response are used, the dilational waves can be captured.
- If high-frequency sensors are used in the measurements, the dilatational wave velocity may be used to compute time delays between signals. Hence, the need to consider dispersive propagation is obviated.

REFERENCES

1. H. Q. Graybill, J. C. Cronon and E. J. Field 1980 *IEEE Transactions PAS* **PAS-99**, 1456–1465. Testing of gas insulated substations and transmission systems.
2. R. T. Harrold 1980 *Conference Rec.*, 1980 *IEEE International Symposium on Electrical Insulation*, New York, USA. 184–189, Acoustic emission signatures of arcs and sparks.
3. N. Okutsu, S. Matsuda, H. Mukae, T. Takahashia and S. Tominaga 1981 *IEEE Transactions PAS*, **PAS-100**, 2733–2739. Pattern recognition of vibrations in metal enclosures of gas insulated equipment and its application.
4. L. E. Lundgaard 1992 *IEEE Insulation Magazine* **8**, 25–31. Partial discharge—part XIII: acoustic partial discharge detection—fundamental consideration.
5. L. E. Lundgaard, M. Runde and B. Skyberg 1990 *IEEE Transactions on Power Delivery* **5**, 1751–1758. Acoustic diagnosis of gas insulated substations: a theoretical and experimental basis.
6. P. Heroux and N. Giao Trinh 1976 *Winter Meeting and Tesla Symposium, IEEE PES*, A76 122.2. A statistical study of electrical and acoustical characteristics of pulsative corona.
7. M. K. Lim 1981 *Applied Acoustics* **14**, 245–253. Corona-type point source for model studies in acoustics.

8. T. BENGTSSON, M. LEIJON, L. MING and B. JOÖNSSON 1995 *IEE Proceedings on Scientific Measurement Technology*, Vol. 142, 85–88. Directivity of acoustic signals from partial discharge in oil.
9. O. C. ZIENKIEWICZ and P. BETTESS 1978 *International Journal for Numerical Methods in Engineering* **13**, 1–16. Fluid–structure dynamic interaction and wave forces: an introduction to numerical treatment.
10. N. GUPTA and T. S. RAMU 1998 *Journal of Computational Acoustics* **6**, 403–419. Estimation of partial discharge parameters in GIS using acoustic emission techniques: a theoretical approach.
11. S. MALLAT and W. L. HWANG 1992 *IEEE Transactions on Information Theory* **38**, 617–643. Singularity detection and processing with wavelets.
12. A. G. PIERSOL 1981 *IEEE Transactions on Acoustics, Speech and Signal Processing* **ASSP-29**, 471–477. Time delay estimation using phase data.
13. B. T. PHUNG, R. E. JAMES, T. R. BLACKBURN and Q. SU 1991 *Proceedings of the Seventh International Symposium on High Voltage Engineering* (*ISH*), 131–134. Partial discharge ultrasonic wave propagation in steel transformer tanks.